

Impact of spin-entropy on the thermoelectric properties of a 2D magnet

Alessandra Canetta,[†] Serhii Volosheniuk,[‡] Sayooj Satheesh,[¶] José Pedro Alvarinhas Batista,[§] Aloïs Castellano,[§] Riccardo Conte,[‡] Daniel G. Chica,^{||} Kenji Watanabe,[⊥] Takashi Taniguchi,[#] Xavier Roy,^{||} Herre S.J. van der Zant,[‡] Marko Burghard,[¶] Matthieu J. Verstraete,^{§,@} and Pascal Gehring^{*,†}

[†]*Institute of Condensed Matter and Nanosciences, Université catholique de Louvain (UCLouvain), 1348 Louvain-la-Neuve, Belgium*

[‡]*Kavli Institute of Nanoscience, Delft University of Technology, 2628CJ Delft, The Netherlands*

[¶]*Max-Planck-Institut für Festkörperforschung, D-70569 Stuttgart, Germany*

[§]*Nanomat/Q-MAT/CESAM and European Theoretical Spectroscopy Facility, Université de Liège, B-4000, Liège, Belgium*

^{||}*Department of Chemistry, Columbia University, New York, NY, 10027 USA*

[⊥]*Research Center for Electronic and Optical Materials, National Institute for Materials Science, 1-1 Namiki, Tsukuba 305-0044, Japan*

[#]*Research Center for Materials Nanoarchitectonics, National Institute for Materials Science, 1-1 Namiki, Tsukuba 305-0044, Japan*

[@]*ITP, Physics Department Utrecht University 3508 TA Utrecht, The Netherlands*

E-mail: pascal.gehring@uclouvain.be

Abstract

Heat-to-charge conversion efficiency of thermoelectric materials is closely linked to the entropy per charge carrier. Thus, magnetic materials are promising building blocks for highly

efficient energy harvesters, as their carrier entropy is boosted by a spin degree of freedom. In this work, we investigate how this spin entropy impacts heat-to-charge conversion in A-type antiferromagnet CrSBr. We perform simultaneous measurements of electrical conductance and thermocurrent while changing magnetic order using temperature and magnetic field as tuning parameters. We find a strong enhancement of the thermoelectric power factor around the Néel temperature. We further reveal that the power factor at low temperature can be increased by up to 600% upon applying a magnetic field. Our results demonstrate that the thermoelectric properties of 2D magnets can be optimized by exploiting the sizeable impact of spin entropy and confirm thermoelectric measurements as a sensitive tool to investigate subtle magnetic phase transitions in low-dimensional magnets.

Keywords

2D magnetism, CrSBr, thermoelectric, entropy

Introduction

The Seebeck coefficient (α) quantifies the electromotive force or gradient of the electrochemical potential $\nabla V = \nabla \tilde{\mu}/q$ developing in a material exposed to a temperature gradient ∇T (Fig. 1), and is the central parameter that determines the efficiency of a thermoelectric device.^{1,2} As the electrochemical potential $\tilde{\mu}$ of a population of electrically charged particles consists of the sum of the chemical potential μ and the electrostatic contribution $q\phi$, the Seebeck coefficient can be written as:³

$$\alpha = -\frac{\partial \tilde{\mu}}{q\partial T} = -\frac{\partial \mu}{q\partial T} - \frac{\partial \phi}{\partial T}, \quad (1)$$

where q is the elementary charge. The second term of equation 1, often referred to as effective Seebeck coefficient, contains dynamical effects linked to scattering/carrier relaxation processes.^{3,4} In contrast, the first component – known as the Kelvin formula^{5,6} – is purely thermodynamic. On the basis of thermodynamic considerations for an electronic system, this term is directly related

to the average entropy transported per charge carrier^{1,7} using the Maxwell equation $\left(\frac{\partial\mu}{\partial T}\right)_N = -\left(\frac{\partial S}{\partial N}\right)_T$, where N is the mean time-averaged population of the system and S is the electronic entropy.⁷⁻⁹ This implies that mechanisms that increase the entropy per carrier can enhance the Seebeck coefficient. In particular, the spin degrees of freedom of carriers in magnetic materials can lead to such increased entropy.^{7,10-12} Fig. 1 illustrates this concept by comparing the Seebeck effect of an antiferromagnet in three temperature regimes, linked to different magnetic phases. In all cases, under open-circuit conditions, a thermally driven diffusion current of charge carriers (red arrows) from the heated region (depicted in orange) to the cold one (in blue) is balanced by a drift current generated by an electric field that builds up inside the material. Moreover, the so-called *spin-entropy*, S_m , in magnetic materials can contribute to their Seebeck effect (bottom panels of Fig. 1).^{1,7} S_m is minimum below the "spin freezing" temperature (Fig. 1a, a special magnetic state in CrSBr, see discussion below). Thermal fluctuations will then increase S_m (Fig. 1b) and it reaches its maximum above the phase transition temperature, as the material enters the paramagnetic state (Fig. 1c).¹

In this context, thanks to their controllable magnetism,¹³⁻¹⁶ two-dimensional (2D) magnets provide an ideal platform to test this effect. Among the layered van der Waals (vdW) materials A-type antiferromagnet CrSBr stands out for its good cleavability as well as its Néel temperature T_N of 132 K, one of the highest reported among vdW antiferromagnets.^{14,17} Compared to ferromagnets, AFM materials offer the possibility to change their spin structure into a field-induced FM configuration upon the application of an external magnetic field, adding a degree of freedom in tuning the electronic and thermoelectric properties.^{18,19} Each CrSBr van der Waals layer consists of two fused buckled planes of CrS, sandwiched between Br atoms and stacked along the c axis (see Fig. 2a).^{14,17} CrSBr is an A-type antiferromagnet, with intralayer ferromagnetic (FM) coupling and interlayer antiferromagnetic (AFM) interaction, and with easy/medium/hard axis coinciding with the crystallographic $b/a/c$ axes, respectively.²⁰ Furthermore, CrSBr shows semiconducting transport properties, with a direct bandgap of $E_G = 1.5$ eV and finite electrical conductivity at low temperature.¹⁸ In particular, thanks to the strong coupling between magnetic ordering and trans-

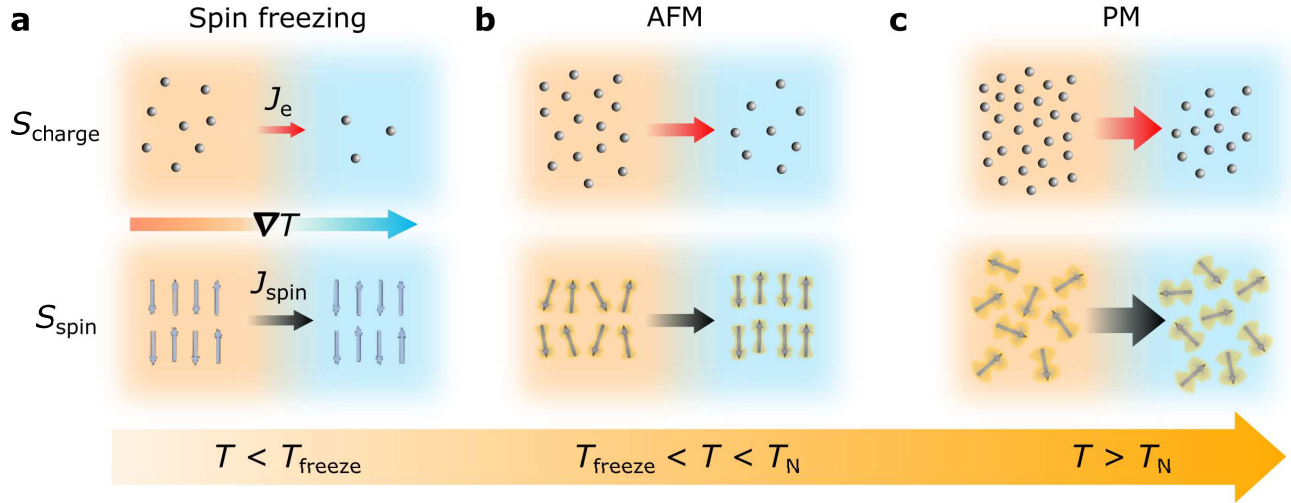


Figure 1: **Seebeck effect in non-magnetic and magnetic materials.** Schematic illustrating the working principle of the Seebeck effect in a material at different magnetic phases. The three images refer to different temperature ranges and consequently magnetic phases: "spin freezing" state (a), antiferromagnetic state (b) and paramagnetic state (c). The top pictures show the thermally-driven diffusion of the charge carriers, of which direction and magnitude are qualitatively indicated by the red arrows. The bottom images show the additional contribution of the spin entropy (S_m) to the Seebeck coefficient. Direction and magnitude of the entropy flow are qualitatively indicated by the black arrows.^{1,7} Temperature ranges are indicated in the large orange arrow at the bottom of the figure, while, in a), the direction of the temperature gradient is illustrated by an orange-to-blue arrow.

port properties in CrSBr, an external magnetic field can be used to alter the electrical resistance, which tends to decrease as the field increases. This comes as a consequence of the reduction of spin fluctuations, and the different interlayer spin-flip scattering between AFM and FM configurations.^{17,18,20,21} While the electrical transport and magnetic properties of this material have been extensively investigated,^{17,18,20–22} the effect of magnetic order on the entropy and thus the thermoelectric properties has not been reported to date.

In this paper we study the impact of electron and spin entropy on the thermoelectric properties of CrSBr thin flakes. To this end, we change magnetic order by varying the sample temperature or by applying an external magnetic field, while simultaneously measuring the electrical and thermoelectric transport properties. We observe a steep increase of the Seebeck coefficient and the thermoelectric power factor with increasing temperature as electrons and spins mobilize, with a local maximum slightly below T_N which we explain by a competition between electronic band

entropy and magnetic entropy in CrSBr. We further reveal that a magnetic field can enhance the power factor by up to 600% at low temperatures. These findings highlight how (spin-)entropy engineering in 2D magnetic materials could be used to realize thermoelectric heat engines with strongly enhanced performance.

Results

To measure the electrical and thermoelectric properties of CrSBr thin flakes we employ a device architecture (Fig. 2b-c) that we recently developed for thermoelectric experiments on single molecule junctions.^{23,24} It consists of pre-patterned contacts, thermometers and microheaters on top of which a CrSBr flake has been stamped using a dry transfer method (see Methods section). A thin hBN flake is used to encapsulate CrSBr to prevent degradation and contamination. An optical micrograph of the final device is shown in Fig. 2d. For a typical measurement (Fig. 2c), an AC current \tilde{I}_h at frequency ω_1 is applied to the microheater which generates a temperature bias ΔT proportional to \tilde{I}_h^2 , therefore having frequency $2\omega_1$. Simultaneously, an AC voltage \tilde{V}_{sd} at frequency $\omega_2 \gg \omega_1$ is applied to the drain contact. The current to ground on the source contact is then demodulated at frequencies ω_2 and $2\omega_1$ to extract the differential conductance $G = \tilde{I}_{sd}/\tilde{V}_{sd}$ and the Seebeck coefficient $\alpha = -\frac{\tilde{V}_{th}}{\Delta T} = -\frac{\tilde{I}_{th}}{G\Delta T}$ (see Supplementary Information section S9 for details on the temperature calibration), respectively. All magnetic fields in this study were applied parallel to the a (medium) axis of CrSBr.

Fig. 2e illustrates the temperature dependence of G and of $\frac{d^2G}{dT^2}$, respectively. G decreases when lowering T , typical for semiconducting materials and in good agreement with previous studies.^{17,18,21} Furthermore, we observe a maximum in G and a sharp dip in $\frac{d^2G}{dT^2}$ around 133 ± 1 K. We associate this value with the Néel temperature T_N , where the transition from the paramagnetic (PM) state (white region) to antiferromagnetic (AFM) (grey region) occurs.^{10,17,18,22,25} Upon further lowering T , G drops by one order of magnitude between T_N and 20 K.²¹ At temperatures lower than $T_{freeze} = 47 \pm 2$ K the appearance of a low-temperature magnetic hidden order has been

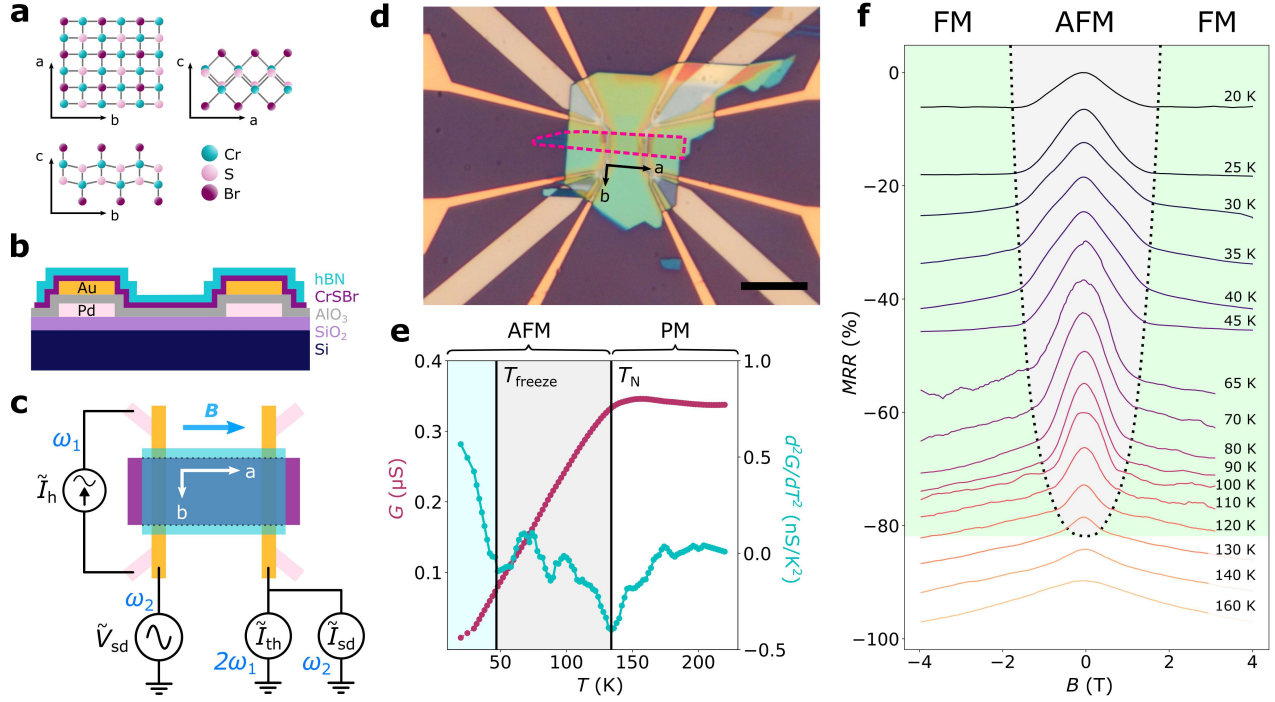


Figure 2: **Crystal structure, measurement setup, and electrical transport of CrSBr.** a) Crystal structure of CrSBr, from the c axis (top left), a axis (top right) and b axis (bottom). Cr, S and Br atoms are represented as cyan, pink and purple spheres, respectively. b) Side view of the schematic of the device. c) Schematic of the setup used for magnetotransport and thermoelectric measurements. d) Optical image of the measured device. The magenta dashed guideline highlights the position of the CrSBr flake, covered by the hBN layer. e) Temperature dependence of the conductance G (purple) and the second derivative of the conductance (cyan). The white region and the light blue/grey region correspond respectively to the paramagnetic (PM) and antiferromagnetic (AFM) phases of CrSBr. f) Magnetoresistance ratio (MRR) versus the applied magnetic field B at different temperatures between 20 and 160 K. An offset of 6% is applied for clarity between each pairs of curves. The AFM and FM magnetic phases are shaded grey and green, respectively. The black dotted line defines the saturation field H_S (see Supplementary Information section S10). Scale bar in (d): $10\ \mu\text{m}$.

reported.^{18,22,26} We do not observe changes in G around T_{freeze} , however, as we will show later, the Seebeck coefficient changes abruptly below this temperature. G values depicted in Fig. 2e are in good agreement with the conductance reported in previous works (^{17,18}).

In Fig. 2f we show the magneto-resistance ratio $MRR = \frac{R(B) - R(B=0)}{R(B=0)} \cdot 100$ at different temperatures between 20 and 160 K (measurements on additional CrSBr devices can be found in the Supplementary Information section S7). Below T_N , for low magnetic fields, spins are coupled an-

tiferromagnetically between layers and aligned along the b (easy) axis (see grey area). As reported previously, this suppresses the interlayer tunneling, and thus leads to an increase in electrical resistance.^{17,18} By raising the applied magnetic field, spins tend to cant: This re-enables interlayer tunneling and therefore lowers the resistance.^{17,18,27} Saturation of the MRR is visible when ferromagnetic order between the layers is established (see green area).¹⁷

Fig. 3a shows the temperature dependence of the Seebeck coefficient simultaneously measured with $G(T)$ (Fig. 2e). The negative sign of α is consistent with the n-type doping typically found in CrSBr, which is attributed to Br vacancies.^{17,28} We observe an overall decrease from $-265 \mu\text{V/K}$ to $-9 \mu\text{V/K}$ when cooling the sample from 200 K to 20 K, which is the base temperature of our experiment. Three areas have been highlighted by means of different colors. In the white region ($T > T_N$), corresponding to the paramagnetic phase, $|\alpha|$ increases as T decreases. $|\alpha|$ reaches its maximum at T_N , stays constant until $T \approx 90$ K, then decreases (overall about 45%) until T_{freeze} (grey region). When cooling below T_{freeze} (light blue area), $|\alpha|$ decreases faster – as can be seen in the first derivative $d\alpha/dT$ (cyan curve) – down to the value of $-9 \mu\text{V/K}$ at 20 K. To explain this behaviour, we performed first principles calculations within the constant relaxation time approximation,²⁹ for a doping of $\sim 8 \cdot 10^{18}$ electrons per cm^3 (see Supplementary Information Fig. S8). In Fig. 3b we compare the AFM ground state, a collinear PM state (averaging special quasirandom structures³⁰), and an interpolation between the two.³¹ The calculations are in good quantitative agreement at low and intermediate temperatures, show the same qualitative extremum and upturn around T_N , but underestimate the upward jump of α in the fully PM phase. Our calculation of the bands in a collinear paramagnetic state produces a smaller Seebeck amplitude (less negative). Freeing the spins to be non collinear PM should produce even more phase space and entropy for the spins, and therefore a larger jump. It should be noted that our first principle model is not suitable to predict $\alpha(T)$ at $T < 50$ K. In this regime, a strong modulation of the carrier concentration is expected which is not accounted for in the calculations.

To gain further evidence for the impact of magnetic order on the thermoelectric properties of CrSBr, we measured the change in Seebeck coefficient as a function of the applied magnetic field.

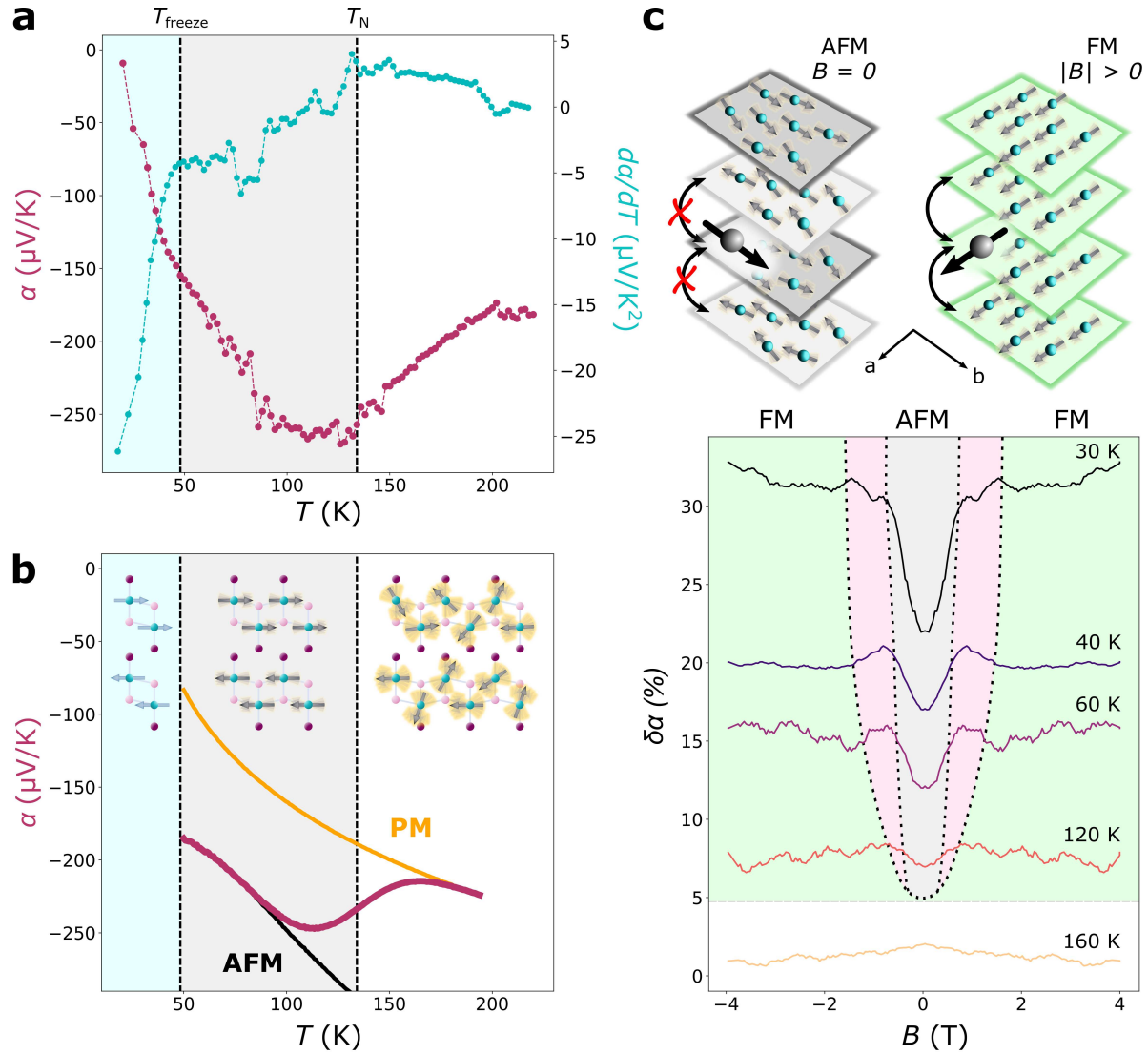


Figure 3: **Magnetic field and temperature dependence of the Seebeck coefficient of CrSBr.** a) Variation of the Seebeck coefficient (purple curve) and its first derivative (cyan curve) at $B = 0T$ as a function of temperature. The temperatures T_N and T_{freeze} separate the graph in three areas, colored respectively in white, grey and light blue. b) First principles Seebeck coefficient as a function of T , for a representative (n-type) doping level, calculated in the AFM (black curve), PM (orange curve), and interpolated magnetic states (purple curve). c) Magneto-Seebeck coefficient as a function of temperature. Each curve is offset by 5% for clarity, and averaged as $\frac{\delta\alpha(B) + \delta\alpha(-B)}{2}$ in order to remove any parasitic effect due to drift in the measurement. The three regions - AFM, transition/canting, FM - are depicted in green, pink and grey, respectively. The field-dependent spin reorientation and interlayer tunneling is illustrated in the top part of the image. The orientation of the crystallographic axes is also reported. An electron residing on one of the layers (dark grey sphere) can tunnel (indicated by the black curved arrows) or not (indicated by the black curved arrows with red X) depending on its spin orientation.

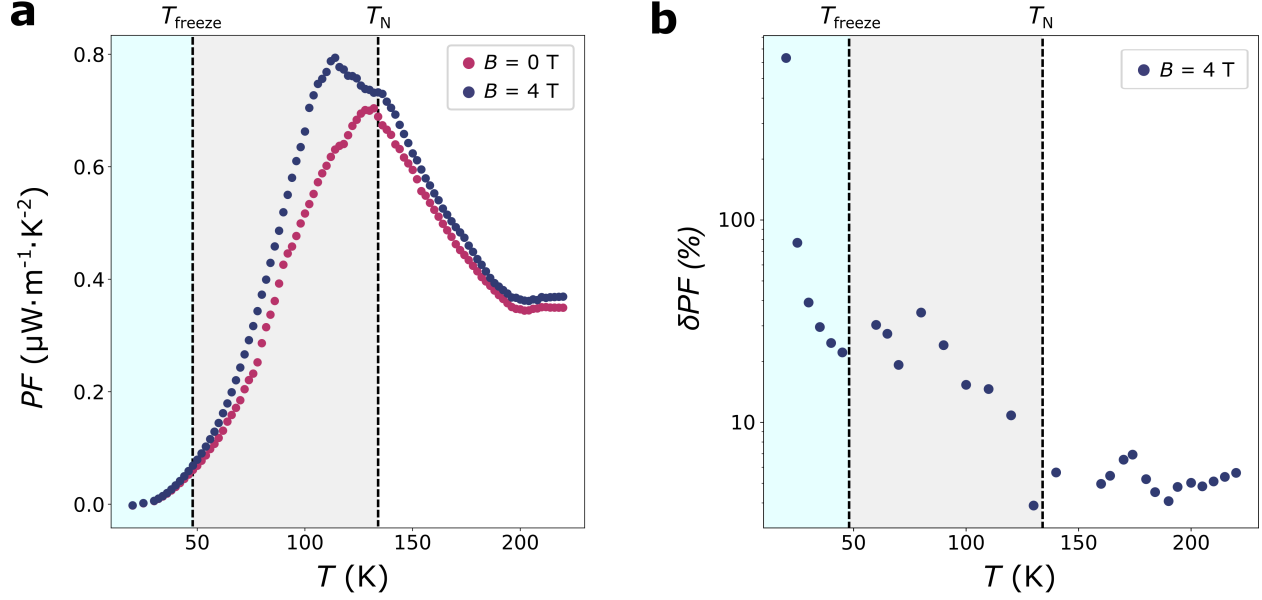


Figure 4: **Field and temperature dependence of the power factor.** a) Temperature dependent power factor, for $B = 0\text{T}$ (purple) and $B = 4\text{T}$ (blue). b) Magneto-power factor (δPF) as a function of temperature, measured at $B = 4\text{T}$.

Fig. 3c shows this magneto-Seebeck coefficient ratio $\delta\alpha = \frac{\alpha(B) - \alpha(B=0)}{\alpha(B=0)} \cdot 100$ versus magnetic field B at temperatures varying between 20 K and 160 K. At 160 K, the flake is in a paramagnetic state and the curve shows almost no variation with applied B field. Below T_N and for small magnetic fields, CrSBr is AFM ordered (grey area) and $\delta\alpha$ is minimum at $B = 0\text{T}$. As the absolute value of B becomes larger, $\delta\alpha$ increases and reaches a local maximum, then decreases until saturating when FM order is established (green area). The areas including the local maxima of $\delta\alpha$ (in pink) can be identified as transition regions, in which the spins are canting from a to b direction due to the application of external B field.²² We observe an increase in $\delta\alpha$ of up to 13% at low T when changing from AFM to FM order.

Fig. 4a displays the temperature-dependent power factor $PF = \alpha^2 \cdot \sigma$, where σ is the electrical conductivity of CrSBr (see Supplementary Information section S3). As part of the figure of merit zT , the power factor helps quantifying the energy harvesting efficiency of the material. As it is also proportional to the maximum achievable output power, it is a useful parameter for quantifying Peltier cooling. At $B = 0$, PF shows a peak of $7\ \mu\text{W m}^{-1}\text{K}^{-2}$ around T_N , where also the

maxima of G and α simultaneously occur. This peak increases in magnitude and shifts to lower temperatures when a magnetic field of $B = 4$ T is applied. Fig. 4b shows the Magneto-power factor $\delta PF = \frac{PF(B=4T) - PF(B=0)}{PF(B=0) \cdot 100}$ as a function of temperature. We observe that the relative change δPF increases with decreasing temperature and reaches values up to 600% at 20K (see Supplementary Information Fig. S7). Below we will discuss that these findings can be explained by the intrinsic band structure of AFM CrSBr, taking into account variations in the entropy linked to the magnetic order.

Discussion

As we described at the beginning of this article, the Seebeck coefficient is closely linked to the entropy S of the system (see Eq. 1).^{8,32} The entropy of a mesoscopic system can be estimated using the Boltzmann formula $S = k_B \ln(\Omega)$, where Ω represents the number of all possible microstates of the system.^{1,33} Here, we assume that Ω contains three main contributions. Ω_p represents the conventional distribution of momenta of the electron gas (electronic band contribution). Then, we take into account a layer degree of freedom Ω_{layer} which quantifies the number of layers a charge carrier can access, as CrSBr is a layered vdW material in which interlayer tunneling is precluded when switching to AFM order.³⁴ Lastly, we include a term Ω_s representing all possible spin configurations, which yields the spin-entropy S_m .³⁵ The sign of this contribution depends on the nature of the d bands hosting the magnetization, which is positive in CrSBr (hole like, from the d band valence electrons).¹ Therefore, the electronic and spin entropy contributions have opposite signs. We now turn back to Fig. 3a, that depicts the temperature dependence of α . As $T \geq T_{\text{freeze}}$, the growth of the Seebeck coefficient abruptly slows down, which is simultaneous with the appearance of a magnetic hidden order below T_{freeze} . Such hidden order was already observed previously by other groups, who associate its origin either to a magnetic coupling between self-trapped defects,¹⁸ the anisotropic structure of CrSBr – which can be seen as weakly and incoherently coupled 1D chains²¹ –, or a spin-dimensionality crossover caused by a slowing down of the magnetic fluc-

tuations (spin freezing).^{22,26} The consequence of the spin freezing phenomenon is that spin fluctuations are fully suppressed ($\Omega_s = 1$) below T_{freeze} , and therefore cannot contribute to the entropy²² to counteract the electronic α .¹ Additionally, interlayer tunneling is suppressed ($\Omega_{\text{layer}} = 1$).^{21,22,26} As the spins mobilize upon heating, their contribution S_m is superimposed on the intrinsic electronic α . Due to the opposite signs of the electronic and spin entropy contributions, their combined action leads to a plateau and turnover when increasing T . At higher temperatures ($T \sim T_N$), two effects cause the reduction in $|\alpha|$ observed in our experiment: Firstly, fluctuations and S_m increase as CrSBr approaches T_N , then saturate in the fully paramagnetic phase;^{10,36} secondly, an increase in carrier concentration decreases the magnitude of α (less negative, see Supplementary Information Fig. S8). The subsequent increase in $|\alpha|$ beyond temperatures of 200 K, as observed in our experiments and predicted by theory, can be attributed to the dominance of Ω_p over the saturated Ω_s in the fully paramagnetic (PM) state.

Fig. 3c illustrates how an external magnetic field B affects α . The application of B along the a direction of CrSBr produces a continuous canting of the spins.¹⁰ Such field-induced spin reorientation initially raises Ω_s , which leads to an increase in $|\alpha|$ (pink shaded areas). When further increasing B , the FM order is established and Ω_s is minimized, reducing $|\alpha|$ again.^{35,37} In addition, the transition from AFM to FM order enables interlayer tunneling and thus raises Ω_{layer} (see Fig. 3c). This could explain the higher α in the FM phase compared to the AFM one and has an important consequence: Since both σ and α simultaneously increase with magnetic field, the relative change of the power factor ($\alpha^2 \sigma$) between AFM and FM order can reach very high values, up to 600% as observed in our experiment (Fig. 4b).

Conclusions

In this work, we investigate the magnetic field and temperature dependent electric and thermoelectric properties of the A-type antiferromagnet CrSBr. We reveal a strong impact of magnetic order on the thermoelectric response of the material, which we attribute to a spin entropy contribution

in the total thermopower. In particular, we detect a peak in both the Seebeck coefficient and the power factor around the magnetic transition temperature T_N . These findings present a potential way to overcome the limits of conventional thermoelectric devices, by employing magnetic materials. While devices based on CrSBr show enhanced thermoelectric properties at cryogenic temperatures, future research should investigate 2D magnets with higher transition temperature to enable room temperature operation. Promising materials that deserve attention are the recently investigated 2D compounds CrTe₂ and Fe₃GaTe₂ with magnetic ordering temperatures > 300 K.^{38,39} To this end, the use of 2D materials adds further benefits, such as the possibility to tune the transition temperature by varying the flake thickness, composition, electrostatic gating, or by producing heterostructures of different layers, in order to yield optimum performance at room temperature.^{40–43}

Experimental

Device fabrication The thermopower devices have been fabricated by standard Electron Beam Lithography (EBL) on a Silicon (Si) wafer with a 285 nm top layer of Silicon Oxide (SiO₂). First, the heaters are fabricated by depositing 3 nm of Titanium (Ti) and 27 nm of Palladium (Pd). Afterwards, the sample is covered by 10 nm of Aluminum Oxide (Al₂O₃) via atomic layer deposition, performed in an Oxford Instruments FlexAL system. Then, 3 nm of Ti and 47 nm of Gold (Au) are deposited as top contacts. Crystals of CrSBr were synthesized using a chemical vapor transport method. This synthetic technique involved the transport of material from 950 °C at the source side to 850 °C at the sink side of a slightly off stoichiometric combination of Cr, S, and CrBr₃ in an evacuated fused silica ampoule. The detailed synthesis and cleaning procedure can be found elsewhere.⁴⁴ CrSBr flakes are mechanically exfoliated using the Scotch tape method^{45,46} and deposited on a PDMS square of approximately 1 mm x 1 mm positioned on a glass slide to facilitate its handling,^{47,48} and transferred onto the pre-patterned contacts. Encapsulation with hBN is then performed by means of the dry transfer method using a PDMS-Polypropylene carbonate (PPC) stamp.^{49,50} The thickness of all flakes is identified by optical contrast and then confirmed by

atomic force microscopy measurements (see Supplementary Information section S2). CrSBr handling is entirely done under inert atmosphere in a N₂ glove box, with <0.5 ppm of O₂ and <0.5 ppm of H₂O content, in order to avoid air degradation and contamination of the sample. More details about the fabrication process can be found in the Supplementary Information (see sections 1-4-5).

Thermoelectric and electrical transport measurements Electrical transport and thermopower measurements were performed in a ⁴He cryostat using home-built ultra-low noise voltage/current sources and pre-amplifiers. We employed a lock-in double-demodulation technique,²⁴ which allows to decouple the thermocurrent \tilde{I}_{th} flowing as a response to a thermal bias ΔT from \tilde{I}_{sd} , the response to a voltage bias \tilde{V}_{sd} .²⁴ To this end, an AC current $\tilde{I}_h = 0.5$ mA (power $P = 0.12$ mW) at frequency $\omega_1 = 3$ Hz is applied to the Pd heater with a Stanford Research SR830 lock-in connected to a current source. Simultaneously, an AC voltage $\tilde{V}_{sd} = 10$ mV at $\omega_2 = 13$ Hz is applied to the drain contact. The current at the source contact is pre-amplified by a low-noise transimpedance amplifier and demodulated at ω_1 and ω_2 to obtain \tilde{I}_{th} and \tilde{I}_{sd} , respectively (see Supplementary Information section 6).

Theory

First Principles Simulations We employ Density Functional Theory^{51,52} as implemented in the ABINIT⁵³ software suite, in a projector augmented wave⁵⁴ basis using JTH⁵⁵ format atomic datasets with plane wave kinetic energy cutoffs of 25 and 30 Ha for the wavefunctions and density (total energies are converged to within 1 meV/atom). The first Brillouin Zone is sampled using a uniform grid of $13 \times 9 \times 3$ points for the ground state and $26 \times 18 \times 6$ to prepare transport calculations. The exchange correlation functional used was the generalized gradient approximation of Perdew Burke and Ernzerhof,⁵⁶ augmented by the Grimme D3 van der Waals dispersion.⁵⁷ The magnetism of Cr necessitates additional Hubbard repulsion in the DFT+U method⁵⁸ (Fully Localized Limit) with a U of 4 eV and J of 1 eV on Cr only (effective U of 3 eV). Most calcu-

lations are performed for collinear spins, and additional checks with non collinear magnetization and spin orbit coupling. The electronic bands are occupied with a Gaussian smearing of 10^{-4} Ha to improve convergence and allow for variable spin polarized occupations, though the final band structures are all semiconducting. The PM high temperature phase is approximated using the Special Quasirandom Structure (SQS) approach³⁰ implemented in the icet package⁵⁹ to generate spin configurations in the infinite temperature limit.⁶⁰ By averaging over 5 different $3 \times 3 \times 2$ supercells with these disordered spins configurations, we obtain a representative electronic DOS and states for the high temperature phase.

Transport The transport coefficients are calculated within the constant relaxation time approximation using the Boltztrap2 code²⁹ for constant doping levels. The Seebeck coefficient is obtained quantitatively as the (unknown) relaxation time drops out of its expression. We infer the experimental doping level ($\sim 8 \cdot 10^{18}$ carriers per cm^3) by comparison of $S(T)$ at low temperature, and consider it constant above T_N as well.

We apply the Boltztrap2 code to the PM approximant SQS supercells, then the results are averaged, to estimate the transport of the PM phase. To compare to the experimental transport measures, we add a crossover/switching from AFM to PM, inspired by Ref.³¹ The switching is chosen as an error function (erf) centered at T_N with a width of 30 K.

Author Contributions

P.G. conceived and supervised the experiments. S.V. fabricated the pre-patterned contacts and performed the experiments. A.C. prepared the CrSBr device, performed the experiments with the support of S.S. and M.B., and evaluated the data. A.C. and P.G. wrote the manuscript. D.C. and X.R. synthesized the CrSBr. K.W. and T.T. provided the hBN. A.Castellano, J.A-B, and M.V. performed the first principles simulations. All authors have given approval to the final version of the manuscript.

Conflicts of interest

There are no conflicts to declare.

Acknowledgement

P.G. acknowledges financial support from the F.R.S.-FNRS of Belgium (FNRS-CQ-1.C044.21-SMARD, FNRS-CDR-J.0068.21-SMARD, FNRS-MIS-F.4523.22-TopoBrain), and from the EU (ERC-StG-10104144-MOUNTAIN). P.G, A.Canetta, A.Castellano, J.A-B, and M.V. acknowledge funding from the Federation Wallonie-Bruxelles through the ARC Grant No. 21/26-116, and from the FWO and FRS-FNRS under the Excellence of Science (EOS) programme (40007563-CONNECT). H.v.d.Z acknowledges support by the FET open project QuIET (Number 767187) and by the Netherlands Organisation for Scientific Research (NWO). K.W. and T.T. acknowledge support from the JSPS KAKENHI (Grant Numbers 21H05233 and 23H02052) and World Premier International Research Center Initiative (WPI), MEXT, Japan for the growth of h-BN crystals. M.B. is grateful for support from the Deutsche Forschungsgemeinschaft (DFG) via Grant BU 1125/11-1. M.V. acknowledges a PRACE award granting access to MareNostrum4 at Barcelona Supercomputing Center (BSC), Spain and Discoverer in SofiaTech, Bulgaria (OptoSpin project id. 2020225411). Synthetic work at Columbia was supported by the National Science Foundation (NSF) through the Columbia Materials Science and Engineering Research Center on Precision-Assembled Quantum Materials (DMR-2011738).

References

- (1) Sun, P.; Kumar, K. R.; Lyu, M.; Wang, Z.; Xiang, J.; Zhang, W. Generic Seebeck effect from spin entropy. *The Innovation* **2021**, *2*, 100101.
- (2) Behnia, K. *Fundamentals of Thermoelectricity*; Oxford University Press, 2015.

- (3) Apertet, Y.; Ouerdane, H.; Goupil, C.; Lecoœur, P. A note on the electrochemical nature of the thermoelectric power. *The European Physical Journal Plus* **2016**, *131*.
- (4) Cai, J.; Mahan, G. D. Effective Seebeck coefficient for semiconductors. *Phys. Rev. B* **2006**, *74*, 075201.
- (5) Chaikin, P. M.; Beni, G. Thermopower in the correlated hopping regime. *Phys. Rev. B* **1976**, *13*, 647–651.
- (6) Peterson, M. R.; Shastry, B. S. Kelvin formula for thermopower. *Phys. Rev. B* **2010**, *82*, 195105.
- (7) Yang, G.; Sang, L.; Zhang, C.; Ye, N.; Hamilton, A.; Fuhrer, M. S.; Wang, X. The role of spin in thermoelectricity. *Nature Reviews Physics* **2023**, *5*, 466–482.
- (8) Pyurbeeva, E.; Mol, J. A.; Gehring, P. Electronic measurements of entropy in meso- and nanoscale systems. *Chemical Physics Reviews* **2022**, *3*, 041308.
- (9) Shastry, B. S. Thermopower in Correlated Systems. *New Materials for Thermoelectric Applications: Theory and Experiment*. Dordrecht, 2013; pp 25–29.
- (10) Tsujii, N.; Nishide, A.; Hayakawa, J.; Mori, T. Observation of enhanced thermopower due to spin fluctuation in weak itinerant ferromagnet. *Science Advances* **2019**, *5*, eaat5935.
- (11) Wang, L.; Zhang, X.; Zhao, L.-D. Evolving Strategies Toward Seebeck Coefficient Enhancement. *Accounts of Materials Research* **2023**, *4*, 448–456.
- (12) Portavoce, A.; Assaf, E.; Bertoglio, M.; Narducci, D.; Bertaina, S. Magnetic moment impact on spin-dependent Seebeck coefficient of ferromagnetic thin films. *Scientific Reports* **2023**, *13*.
- (13) Yao, Y.; Zhan, X.; Sendeku, M. G.; Yu, P.; Dajan, F. T.; Zhu, C.; Li, N.; Wang, J.; Wang, F.; Wang, Z.; He, J. Recent progress on emergent two-dimensional magnets and heterostructures. *Nanotechnology* **2021**, *32*, 472001.

- (14) Jiang, X.; Liu, Q.; Xing, J.; Liu, N.; Guo, Y.; Liu, Z.; Zhao, J. Recent progress on 2D magnets: Fundamental mechanism, structural design and modification. *Applied Physics Reviews* **2021**, *8*, 031305.
- (15) Burch, K.; Mandrus, D.; Park, J.-G. Magnetism in two-dimensional van der Waals materials. *Nature* **2018**, *563*.
- (16) Cortie, D. L.; Causer, G. L.; Rule, K. C.; Fritzsche, H.; Kreuzpaintner, W.; Klose, F. Two-Dimensional Magnets: Forgotten History and Recent Progress towards Spintronic Applications. *Advanced Functional Materials* **2020**, *30*, 1901414.
- (17) Telford, E. J.; Dismukes, A. H.; Lee, K.; Cheng, M.; Wieteska, A.; Bartholomew, A. K.; Chen, Y.-S.; Xu, X.; Pasupathy, A. N.; Zhu, X.; Dean, C. R.; Roy, X. Layered Antiferromagnetism Induces Large Negative Magnetoresistance in the van der Waals Semiconductor CrSBr. *Advanced Materials* **2020**, *32*, 2003240.
- (18) Telford, E. et al. Coupling between magnetic order and charge transport in a two-dimensional magnetic semiconductor. *Nature Materials* **2022**, *21*, 754–760.
- (19) Bauer, G. E. W.; Saitoh, E.; van Wees, B. J. Spin caloritronics. *Nature Materials* **2012**, *11*, 391–399.
- (20) Lee, K.; Dismukes, A. H.; Telford, E. J.; Wiscons, R. A.; Wang, J.; Xu, X.; Nuckolls, C.; Dean, C. R.; Roy, X.; Zhu, X. Magnetic Order and Symmetry in the 2D Semiconductor CrSBr. *Nano Letters* **2021**, *21*, 3511–3517, PMID: 33856213.
- (21) Wu, F.; Gutiérrez-Lezama, I.; López-Paz, S. A.; Gibertini, M.; Watanabe, K.; Taniguchi, T.; von Rohr, F. O.; Ubrig, N.; Morpurgo, A. F. Quasi-1D Electronic Transport in a 2D Magnetic Semiconductor. *Advanced Materials* **2022**, *34*, 2109759.
- (22) López Paz, S.; Guguchia, Z.; Pomjakushin, V.; Witteveen, C.; Cervellino, A.; Luetkens, H.;

- Casati, N.; Morpurgo, A.; Rohr, F. Dynamic magnetic crossover at the origin of the hidden-order in van der Waals antiferromagnet CrSBr. *Nature Communications* **2022**, *13*.
- (23) Gehring, P.; van der Star, M.; Evangelini, C.; Le Roy, J. J.; Bogani, L.; Kolosov, O. V.; van der Zant, H. S. J. Efficient heating of single-molecule junctions for thermoelectric studies at cryogenic temperatures. *Applied Physics Letters* **2019**, *115*, 073103.
- (24) Gehring, P.; Sowa, J.; Hsu, C.; Bruijckere, J.; Star, M.; Le Roy, J.; Bogani, L.; Gauger, E.; Zant, H. Complete mapping of the thermoelectric properties of a single molecule. *Nature Nanotechnology* **2021**, *16*, 1–5.
- (25) Liu, W.; Guo, X.; Schwartz, J.; Xie, H.; Dhale, N. U.; Sung, S. H.; Kondusamy, A. L. N.; Wang, X.; Zhao, H.; Berman, D.; Hovden, R.; Zhao, L.; Lv, B. A Three-Stage Magnetic Phase Transition Revealed in Ultrahigh-Quality van der Waals Bulk Magnet CrSBr. *ACS Nano* **2022**, *16*, 15917–15926, PMID: 36149801.
- (26) Boix-Constant, C.; Mañas-Valero, S.; Ruiz, A. M.; Rybakov, A.; Konieczny, K. A.; Pillet, S.; Baldoví, J. J.; Coronado, E. Probing the Spin Dimensionality in Single-Layer CrSBr Van Der Waals Heterostructures by Magneto-Transport Measurements. *Advanced Materials* **2022**, *34*, 2204940.
- (27) Ye, C.; Wang, C.; Wu, Q.; Liu, S.; Zhou, J.; Wang, G.; Söll, A.; Sofer, Z.; Yue, M.; Liu, X.; Tian, M.; Xiong, Q.; Ji, W.; Renshaw Wang, X. Layer-Dependent Interlayer Antiferromagnetic Spin Reorientation in Air-Stable Semiconductor CrSBr. *ACS Nano* **2022**, *16*, 11876–11883, PMID: 35588189.
- (28) Klein, J. et al. The Bulk van der Waals Layered Magnet CrSBr is a Quasi-1D Material. *ACS Nano* **2023**, *17*, 5316–5328, PMID: 36926838.
- (29) Madsen, G. K.; Carrete, J.; Verstraete, M. BoltzTraP2, a program for interpolating band structures and calculating semi-classical transport coefficients. *Computer Physics Communications* **2018**, *231*, 140 – 145.

- (30) Zunger, A.; Wei, S.-H.; Ferreira, L. G.; Bernard, J. E. Special quasirandom structures. *Physical Review Letters* **1990**, *65*, 353–356.
- (31) Körmann, F.; Grabowski, B.; Dutta, B.; Hickel, T.; Mauger, L.; Fultz, B.; Neugebauer, J. Temperature Dependent Magnon-Phonon Coupling in bcc Fe from Theory and Experiment. *Physical Review Letters* **2014**, *113*.
- (32) Sun, Z.; Wang, H.; Wang, A.; Lei, B.; Zhuo, W.; Yu, F.; Zhou, X.; Ying, J.; Xiang, Z.; Wu, T.; Chen, X. Large Thermopower Enhanced by Spin Entropy in Antiferromagnet EuMnSb₂. *Advanced Functional Materials* **2022**, *32*, 2202188.
- (33) Demirel, Y.; Gerbaud, V. In *Nonequilibrium Thermodynamics (Fourth Edition)*, fourth edition ed.; Demirel, Y., Gerbaud, V., Eds.; Elsevier, 2019; pp 603–662.
- (34) Wilson, N.; Lee, K.; Cenker, J.; Xie, K.; Dismukes, A.; Telford, E.; Fonseca, J.; Sivakumar, S.; Dean, C.; Cao, T.; Roy, X.; Xu, X.; Zhu, X. Interlayer electronic coupling on demand in a 2D magnetic semiconductor. *Nature Materials* **2021**, *20*, 1–6.
- (35) Wang, Y.; Rogado, N. S.; Cava, R. J.; Ong, N. P. Spin entropy as the likely source of enhanced thermopower in Na_xCo₂O₄. *Nature* **2003**, *423*, 425–428.
- (36) Okabe, T. Spin-fluctuation drag thermopower of nearly ferromagnetic metals. *Journal of Physics: Condensed Matter* **2010**, *22*, 115604.
- (37) Bonner, J. C.; Fisher, M. E. The Entropy of an Antiferromagnet in a Magnetic Field. *Proceedings of the Physical Society* **1962**, *80*, 508.
- (38) Wu, H.; Zhang, W.; Yang, L.; Wang, J.; Li, J.; Li, L.; Gao, Y.; Zhang, L.; Du, J.; Shu, H.; Chang, H. Strong intrinsic room-temperature ferromagnetism in freestanding non-van der Waals ultrathin 2D crystals. *Nature Communications* **2021**, *12*.
- (39) Zhang, X. et al. Room-temperature intrinsic ferromagnetism in epitaxial CrTe₂ ultrathin films. *Nature Communications* **2021**, *12*, 2492.

- (40) Li, D.; Gong, Y.; Chen, Y.-X.; Lin, J.; Khan, Q.; Zhang, Y.; Li, Y.; Xie, H. Recent Progress of Two-Dimensional Thermoelectric Materials. *Nano-Micro Letters* **2020**, *12*, 36.
- (41) Razeghi, M.; Spiece, J.; Oğuz, O.; Pehlivanoglu, D.; Huang, Y.; Sheraz, A.; Başçı, U.; Dobson, P.; Weaver, J.; Gehring, P.; Kasirga, S. Single-material MoS₂ thermoelectric junction enabled by substrate engineering. *npj 2D Materials and Applications* **2023**, *7*.
- (42) Tu, S. et al. Record thermopower found in an IrMn-based spintronic stack. *Nature Communications* **2020**, *11*.
- (43) Oh, J.; Kim, Y.; Chung, S.; Kim, H.; Son, J. G. Fabrication of a MoS₂/Graphene Nanoribbon Heterojunction Network for Improved Thermoelectric Properties. *Advanced Materials Interfaces* **2019**, *6*, 1901333.
- (44) Scheie, A.; Ziebel, M.; Chica, D. G.; Bae, Y. J.; Wang, X.; Kolesnikov, A. I.; Zhu, X.; Roy, X. Spin Waves and Magnetic Exchange Hamiltonian in CrSBr. *Advanced Science* **2022**, *9*, 2202467.
- (45) Novoselov, K. S.; Geim, A. K.; Morozov, S. V.; Jiang, D.; Zhang, Y.; Dubonos, S. V.; Grigorieva, I. V.; Firsov, A. A. Electric Field Effect in Atomically Thin Carbon Films. *Science* **2004**, *306*, 666–669.
- (46) Novoselov, K. S.; Jiang, D.; Schedin, F.; Booth, T. J.; Khotkevich, V. V.; Morozov, S. V.; Geim, A. K. Two-dimensional atomic crystals. *Proceedings of the National Academy of Sciences* **2005**, *102*, 10451–10453.
- (47) Castellanos-Gomez, A.; Buscema, M.; Zant, H.; Steele, G. Deterministic transfer of two-dimensional materials by all-dry viscoelastic stamping. *2D Materials* **2013**, *1*.
- (48) Frisenda, R.; Navarro-Moratalla, E.; Gant, P.; Perez de Lara, D.; Jarillo-Herrero, P.; Gorbachev, R.; Castellanos-Gomez, A. Recent progress in the assembly of nanodevices and van

- der Waals heterostructures by deterministic placement of 2D materials. *Chemical Society Reviews* **2017**, *47*.
- (49) Kinoshita, K.; Moriya, R.; Onodera, M.; Wakafuji, Y.; Masubuchi, S.; Watanabe, K.; Taniguchi, T.; Machida, T. Dry release transfer of graphene and few-layer h-BN by utilizing thermoplasticity of polypropylene carbonate. *npj 2D Materials and Applications* **2019**, *3*.
- (50) Wang, L.; Meric, I.; Huang, P. Y.; Gao, Q.; Gao, Y.; Tran, H.; Taniguchi, T.; Watanabe, K.; Campos, L. M.; Muller, D. A.; Guo, J.; Kim, P.; Hone, J.; Shepard, K. L.; Dean, C. R. One-Dimensional Electrical Contact to a Two-Dimensional Material. *Science* **2013**, *342*, 614–617.
- (51) Hohenberg, P.; Kohn, W. Inhomogeneous Electron Gas. *Phys. Rev.* **1964**, *136*, 864–871.
- (52) Kohn, W.; Sham, L. J. Self-Consistent Equations Including Exchange and Correlation Effects. *Phys. Rev.* **1965**, *140*, A 1133 – A 1138.
- (53) Gonze, X.; Amadon, B.; Antonius, G.; Arnardi, F.; Baguet, L.; Beuken, J.-M.; Bieder, J.; Bottin, F.; Bouchet, J.; Bousquet, E.; others The ABINIT project: Impact, environment and recent developments. *Computer Physics Communications* **2020**, *248*, 107042.
- (54) Blöchl, P. E. Projector augmented-wave method. *Phys. Rev. B* **1994**, *50*, 17953–17979.
- (55) Jollet, F.; Torrent, M.; Holzwarth, N. Generation of Projector Augmented-Wave atomic data: A 71 element validated table in the XML format. *Computer Physics Communications* **2014**, *185*, 1246–1254.
- (56) Perdew, J. P.; Burke, K.; Ernzerhof, M. Generalized Gradient Approximation Made Simple. *Phys. Rev. Lett.* **1996**, *77*, 3865.
- (57) Grimme, S.; Antony, J.; Ehrlich, S.; Krieg, H. A consistent and accurate ab initio parametrization of density functional dispersion correction (DFT-D) for the 94 elements H-Pu. *The Journal of Chemical Physics* **2010**, *132*, 154104.

- (58) Anisimov, V.; Zaanen, J.; Andersen, O. Band theory and Mott insulators: Hubbard U instead of Stoner I. *Phys. Rev. B* **1991**, *44*, 943.
- (59) Ångqvist, M.; Muñoz, W. A.; Rahm, J. M.; Fransson, E.; Durniak, C.; Rozyczko, P.; Rod, T. H.; Erhart, P. ICET – A Python Library for Constructing and Sampling Alloy Cluster Expansions. *Advanced Theory and Simulations* **2019**, *2*.
- (60) Abrikosov, I.; Ponomareva, A.; Steneteg, P.; Barannikova, S.; Alling, B. Recent progress in simulations of the paramagnetic state of magnetic materials. *Current Opinion in Solid State and Materials Science* **2016**, *20*, 85–106.